nature communications

Article

https://doi.org/10.1038/s41467-025-63097-8

A lithography-free approach to polaritonic Luneburg lenses

Received: 10 January 2025

Accepted: 4 August 2025

Published online: 20 August 2025

Check for updates

Zhenyang Cui[1,2,3,8], Youning Gong[4,8], Wenzhi Yu[5], Sihao Xia[1,2,3], Zhiwei He[1,2,3], Xingyu Tang[1,2,3], Bin Zheng[1,2,3], Huaping Wang[1,2,3], Weiliang Ma[6,7], Yupeng Zhang[4] ✉, Hongsheng Chen[1,2,3] ✉ & Yingjie Wu[1,2,3] ✉

Planar polaritonic lenses, achieved by precisely controlling interface polaritons, hold significant promise for subwavelength light focusing. While most existing designs rely on polariton interference or refraction, creating gradient-index polaritonic lenses remains a substantial challenge due to the lack of practical and cost-effective fabrication methods. Here, we introduce a lithography-free approach for producing polaritonic lenses with gradient effective refractive indices by engineering the dielectric environment of polaritons. This method involves in situ transformation of polymer microspheres into spherical caps through controlled melting, allowing the fabrication of polaritonic Luneburg lenses with focal spots as small as $\lambda_0/18$, where λ_0 is the free-space wavelength. Our approach could also apply to other gradient-index polaritonic lenses, such as Maxwell fisheye lenses and Mikaelian lenses, based on a wide range of in-plane isotropic polariton modes. By circumventing traditional nanofabrication constraints, this versatile and cost-effective technique offers a promising platform for developing polaritonic devices, which are essential for future polaritonic systems and integrated circuits.

Polaritons, hybrid modes of photons coupled with material excitations, offer a powerful platform for manipulating light beyond the diffraction limit by confining it to surfaces or interfaces[1–4]. This strong confinement, typically extending hundreds of nanometers out of plane[5], makes polaritons particularly promising for on-chip photonic applications compatible with integrated circuits[6,7]. Various planar polaritonic devices, including resonators[8–14], waveguides[15–18], and prisms[19–21], have been realised, laying the foundation for next-generation electro-optical and all-optical systems.

One of the most striking applications of polaritons is in planar polaritonic lenses, which can focus light with subwavelength resolution. Existing planar polaritonic lenses have been developed through either polariton interference[22–25] or refraction[26–29]. Refractive lenses work by shaping the polariton wavefront via impedance interfaces, enabling the creation of gradient-index lenses. However, achieving these lenses with nanometallic antennas remains a challenge. Two main strategies have been proposed to create gradient refractive polaritonic lenses: modifying the polaritonic material itself[19,30,31] or engineering the surrounding dielectric environment[32–36].

Material-based methods, such as tailoring the thickness of polaritonic materials (d_{pm}), have been employed to shape and focus waveguide-like volume-confined polaritons, where the polariton

[1]State Key Laboratory of Extreme Photonics and Instrumentation, ZJU-Hangzhou Global Scientific and Technological Innovation Center, Zhejiang University, Hangzhou, China. [2]International Joint Innovation Center, The Electromagnetics Academy at Zhejiang University, Zhejiang University, Haining, China. [3]Key Lab. of Advanced Micro/Nano Electronic Devices & Smart Systems of Zhejiang, Jinhua Institute of Zhejiang University, Zhejiang University, Jinhua, China. [4]State Key Laboratory of Radio Frequency Heterogeneous Integration, College of Physics and Optoelectronic Engineering, Shenzhen University, Shenzhen, China. [5]Siscan Technology Co. Ltd, Suzhou, China. [6]National Engineering Research Center of Electromagnetic Radiation Control Materials, University of Electronic Science and Technology of China, Chengdu, China. [7]Key Laboratory of Multi-spectral Absorbing Materials and Structures of Ministry of Education, University of Electronic Science and Technology of China, Chengdu, China. [8]These authors contributed equally: Zhenyang Cui, Youning Gong.
✉e-mail: ypzhang@szu.edu.cn; hansomchen@zju.edu.cn; yingjie.wu@zju.edu.cn

https://doi.org/10.1038/s41467-025-63097-8

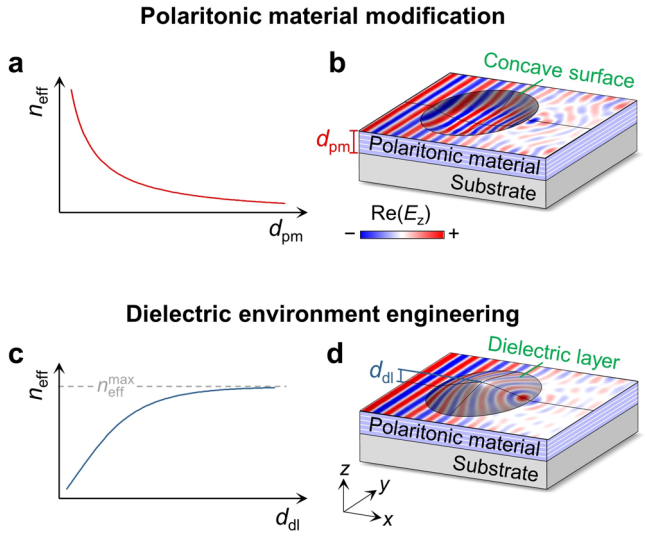

Fig. 1 | Two strategies for realizing gradient-index polaritonic lenses. a Inverse relationship between the effective refractive index (n_{eff}) and the thickness of the polaritonic material (d_{pm}) that supports volume-confined polaritons. **b** Schematic of a polaritonic Luneburg lens formed by spatially varying d_{pm}. A representative field distribution, denoted by the real part of the electric field in the z direction, Re(E_z), is overlaid on the surface of hBN. **c** Nonlinear dependence of n_{eff} on the thickness of the dielectric layer (d_{dl}), exhibiting a maximum value, n_{eff}^{max}. **d** A polaritonic Luneburg lens developed through dielectric environment engineering.

momentum (q) is inversely proportional to d_{pm}[30,31]. Figure 1a shows the relation between d_{pm} and the effective refractive index (n_{eff}), defined as q/q_0, where q_0 is the polariton momentum in the absence of modifications. This phenomenon enables the creation of gradient polaritonic lenses with concave surfaces, such as the Luneburg lens in Fig. 1b, where polaritons propagating along the x direction are focused at the lens rim.

An alternative and widely applicable approach involves engineering the dielectric environment. For example, placing a dielectric layer atop a polaritonic material can modify the polariton dispersion, typically resulting in an increase in n_{eff} with the dielectric layer thickness (d_{dl}), asymptotically approaching a maximum value (n_{eff}^{max}). This relationship (Fig. 1c), although nonlinear[32,33], can be harnessed to create gradient-index lenses. Polaritonic Luneburg and Eaton lenses have been successfully fabricated using grey-scale electron beam lithography (EBL) to pattern photoresist layers, such as polymethyl methacrylate (PMMA), of spatially varying thickness[34,35]. A schematic of a Luneburg lens fabricated by this method is shown in Fig. 1d. While effective, these fabrication methods are limited by the complexity and high cost of nanofabrication, which often require precise etching or patterning.

Here, we present a lithography-free approach for fabricating polaritonic Luneburg lenses with gradient n_{eff}. This method leverages dielectric environment engineering, wherein polymer microspheres are reshaped into spherical caps via controlled thermal treatment. The resulting thickness profiles, governed by a balance between spreading and evaporation dynamics, closely approximate the ideal gradient required for polaritonic Luneburg lenses, yielding focal spots as small as $\lambda_0/18$, where λ_0 is the free-space wavelength. Beyond Luneburg lenses, this method is also adaptable to other gradient-index lenses, including Maxwell fisheye and Mikaelian lenses, applicable across a wide range of in-plane isotropic polariton modes. The simplicity, versatility, and scalability of this technique offer a promising pathway for advancing subwavelength polaritonic components.

Results

Gradient indices from dielectric environment engineering

The propagation of polaritons is significantly influenced by the surrounding dielectric environment, particularly the dielectric permittivities of the substrate (ε_{sub}) and superstrate (ε_{sup}). We illustrate this by considering phonon polaritons (PhPs) in hexagonal boron nitride (hBN) and comparing two superstrates, air and PMMA. The dispersion relations for these systems are shown in Fig. 2a, derived from a waveguide-like eigenequation for a three-layer structure (see Supplementary Note 1 and Supplementary Fig. 1), with the hBN thickness (d_{hBN}) fixed at 50 nm. Notably, the PMMA superstrate results in a higher in-plane momentum within the frequency range between the transverse optical (ω_{TO}, 1340 cm^{-1}) and longitudinal optical phonon frequencies (ω_{LO}, 1630 cm^{-1}) of hBN, corresponding to the type II Reststrahlen band. This effect arises from PMMA's larger dielectric permittivity ($\varepsilon_{PMMA} > \varepsilon_{air}$) as depicted in Supplementary Fig. 2. Simulation results in the insets of Fig. 2a confirm that a PMMA superstrate enables a shorter polariton wavelength (λ_p) at a given frequency ($\omega = 1500\ cm^{-1}$).

When an hBN slab is overlaid with a PMMA layer of finite thickness (d_{PMMA}), the polariton dispersion in this four-layer structure lies between those of the three-layer structures with either air or PMMA as the superstrate, as indicated by the blue region in Fig. 2a. The PMMA thickness thus serves as a key tuning parameter for continuously engineering polariton dispersions. As illustrated in Fig. 2b, when $d_{PMMA} = 0$, the system resembles a three-layer structure with an air superstrate, while increasing d_{PMMA} progressively elevates q, approaching the value associated with a PMMA superstrate. This trend is further supported by the simulation result in the inset of Fig. 2b, where λ_p gradually decreases along a PMMA taper.

The d_{PMMA}-dependent dispersions of PhPs offer a promising strategy for designing refractive polaritonic lenses with gradient n_{eff}, as shown in Fig. 2c. A similar effect has also been observed in PMMA/gold and SiO_2/graphene structures that rely on surface-confined plasmon polaritons[32,34,35,37]. By contrast, we employ PhPs supported by polar dielectrics, which exhibit lower losses in the mid-infrared range, facilitating more efficient visualisation of near-field distributions at room temperature (see below). Furthermore, unlike surface modes, PhPs in hBN are volume-confined modes, with their electromagnetic fields concentrated inside the thin slab. This property renders n_{eff} thickness dependence, with thinner hBN slabs leading to a more rapid increase in n_{eff} as d_{PMMA} increases, as shown in Fig. 2d. However, the n_{eff}^{max} is solely determined by the dielectric permittivities of the system, as given by:

$$n_{eff}^{max} \approx \frac{\varepsilon_{sub} + \varepsilon_{PMMA}}{\varepsilon_{sub} + \varepsilon_{sup}} \quad (1)$$

at the frequency close to ω_{TO} of hBN (Supplementary Note 1). Specifically, n_{eff}^{max} can reach up to 1.69 for both the hBN slab ($d_{hBN} = 50$ nm) and hBN monolayer supported by a SiO_2 substrate (Supplementary Fig. 3). Even a higher n_{eff} could be achieved in polaritonic systems consisting of different materials, as demonstrated by the calculated n_{eff} as a function of the permittivities of the dielectric layer (ε_{dl}, Fig. 2e) and the substrate (Fig. 2f). These results outline a clear strategy for designing gradient polaritonic lenses through careful parameter selection.

Lithography-free approach for gradient polaritonic lenses

Previous methods for fabricating gradient polaritonic lenses primarily rely on grey-scale EBL, which involves patterning a spin-coated photoresist film to create spatially varying thicknesses after the lift-off process[34]. This approach requires precise control over the lithographic

https://doi.org/10.1038/s41467-025-63097-8

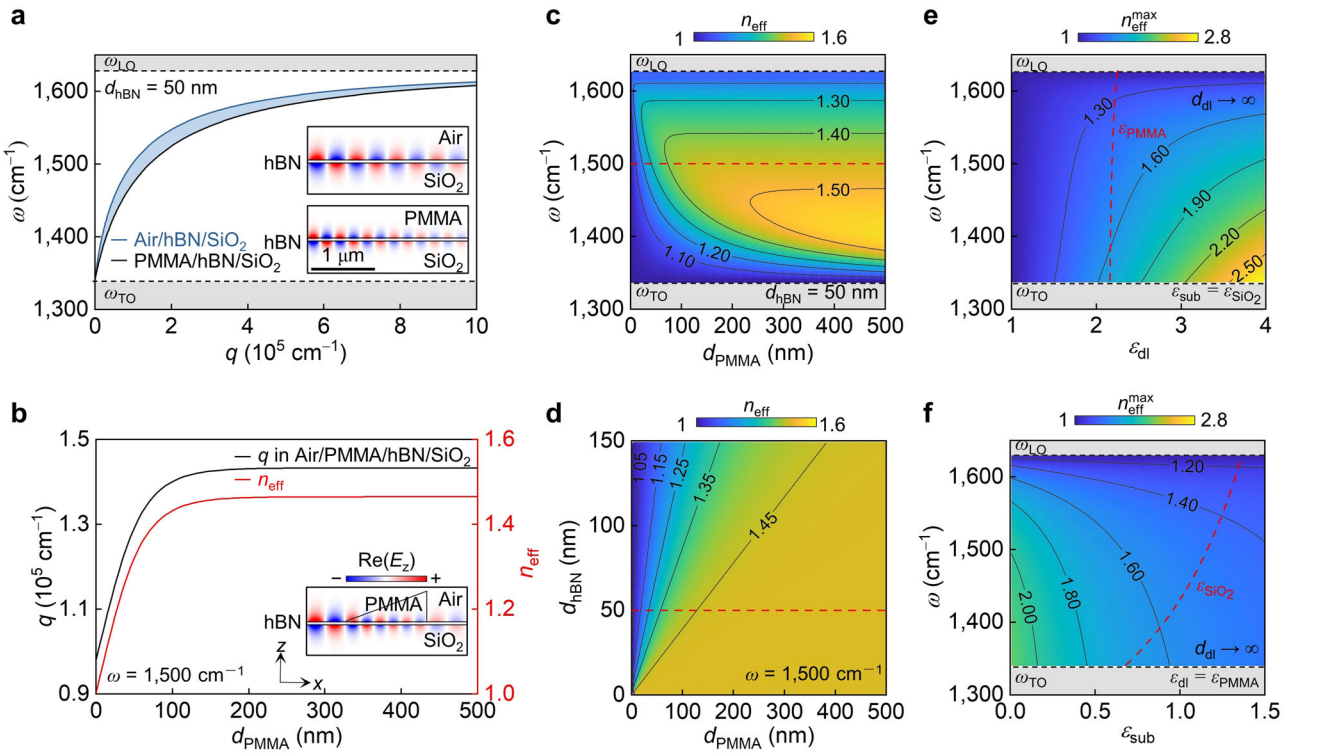

Fig. 2 | Gradient effective refractive indices enabled by dielectric environment engineering. a Calculated dispersion relations of phonon polaritons in air/hBN/SiO_2 and PMMA/hBN/SiO_2 three-layer structures. Insets show simulated field distributions at the frequency (ω) of 1500 cm^{-1}, with the hBN slab thickness (d_{hBN}) set to 50 nm. **b** Polariton momentum (q) and effective refractive index (n_{eff}) as a function of PMMA thickness (d_{PMMA}) in an air/PMMA/hBN/SiO_2 four-layer structure. Inset shows the gradually decreasing polariton wavelengths across a PMMA taper. **c** Calculated n_{eff} as a function of d_{PMMA} at different frequencies. **d** Tuning n_{eff} through adjustments in both d_{hBN} and d_{PMMA}. Dependence of the maximum refractive index (n_{eff}^{max}) on the dielectric permittivities of the dielectric layer (ε_{dl}, **e**) and the substrate (ε_{sub}, **f**), under the approximation of the infinite dielectric layer thickness ($d_{dl} \to \infty$). Red curves respectively indicate the dielectric permittivities of PMMA (ε_{PMMA}) and SiO_2 (ε_{SiO_2}) employed in theoretical analysis.

dose, particularly for nanoscale structures, which complicates the fabrication process. To address these challenges and enhance fabrication efficiency, we introduce a lithography-free method that utilises controlled melting of pre-prepared polymer microspheres. As illustrated schematically in Fig. 3a, a drop of PMMA microsphere suspension is deposited onto a SiO_2/Si substrate supporting hBN slabs. After solvent evaporation, the microspheres adhere to the hBN surface. The sample is then heated to 250 °C and maintained for several hours, depending on the sizes of the hBN slabs and microspheres, allowing for the melting and controlled deformation of the PMMA microspheres. Upon cooling to room temperature, the melted PMMA solidifies into microstructures with gradient thicknesses, which can serve as gradient-index polaritonic lenses. See Methods for detailed fabrication procedures.

The morphological evolution of a PMMA microsphere with an initial radius (r_0) of 0.6 μm was investigated using optical microscopy and atomic force microscopy (AFM). Figure 3b displays optical microscopy images (bottom panel) alongside corresponding AFM profiles (top panel) of a PMMA microsphere on an hBN slab at various time intervals, revealing its deformation during thermal treatment. This behaviour is reminiscent of a water droplet spreading on a hot hydrophilic surface. Figure 3c quantifies the evolution, showing an initial increase in lateral radius followed by a subsequent reduction, accompanied by a monotonic decrease in height. These trends are further supported by volume (V) measurements shown in Supplementary Fig. 4. Additional experiments with finer temporal resolution on two other samples are provided in Supplementary Fig. 5. While the total evaporation time depends on microsphere size, all samples exhibit a consistent deformation pattern: an initial rapid lateral expansion within the first minute, followed by a slower increase, and a pronounced shrinkage around 2 h. This consistency underscores the reproducibility and robustness of our fabrication method.

Thermogravimetric analysis (TGA) of the PMMA microsphere suspension in air (Fig. 3d) reveals a glass transition temperature (T_g) of ~71 °C, notably lower than that of bulky PMMA (100–120 °C), due to the size-dependent T_g of PMMA[38]. Following an initial weight loss attributed to solvent evaporation, the sample mass remains stable up to 250 °C, indicating the onset of degradation and evaporation of PMMA. Combining the TGA data with the observed morphological evolution, we conclude that the final geometry of the PMMA microstructure is governed by the interplay between spreading and evaporation. Owing to the rapid heating rate, evaporation begins early in the process and proceeds concurrently with spreading. Therefore, the turning point in measured radius in Fig. 3c and Supplementary Fig. 5 does not correspond to the onset of evaporation, but rather the point at which volume loss due to evaporation begins to dominate over spreading-induced expansion. Conversely, the initial radius expansion reflects the dominance of spreading in the early stages. The competition between these two processes, compounded by the temperature-dependent viscosity of PMMA, renders quantitative modelling of this non-equilibrium transformation particularly challenging[39]. To provide qualitative insight, Fig. 3e schematically illustrates the morphological evolution of a PMMA microsphere during thermal treatment, alongside time-dependent profiles of temperature and volume.

Building on the observed morphological evolution of the PMMA microsphere, we develop a simple model to describe the geometry of PMMA microstructures during thermal treatment. The thicknesses of the PMMA microstructures, extracted from AFM profiles in Fig. 3b, are

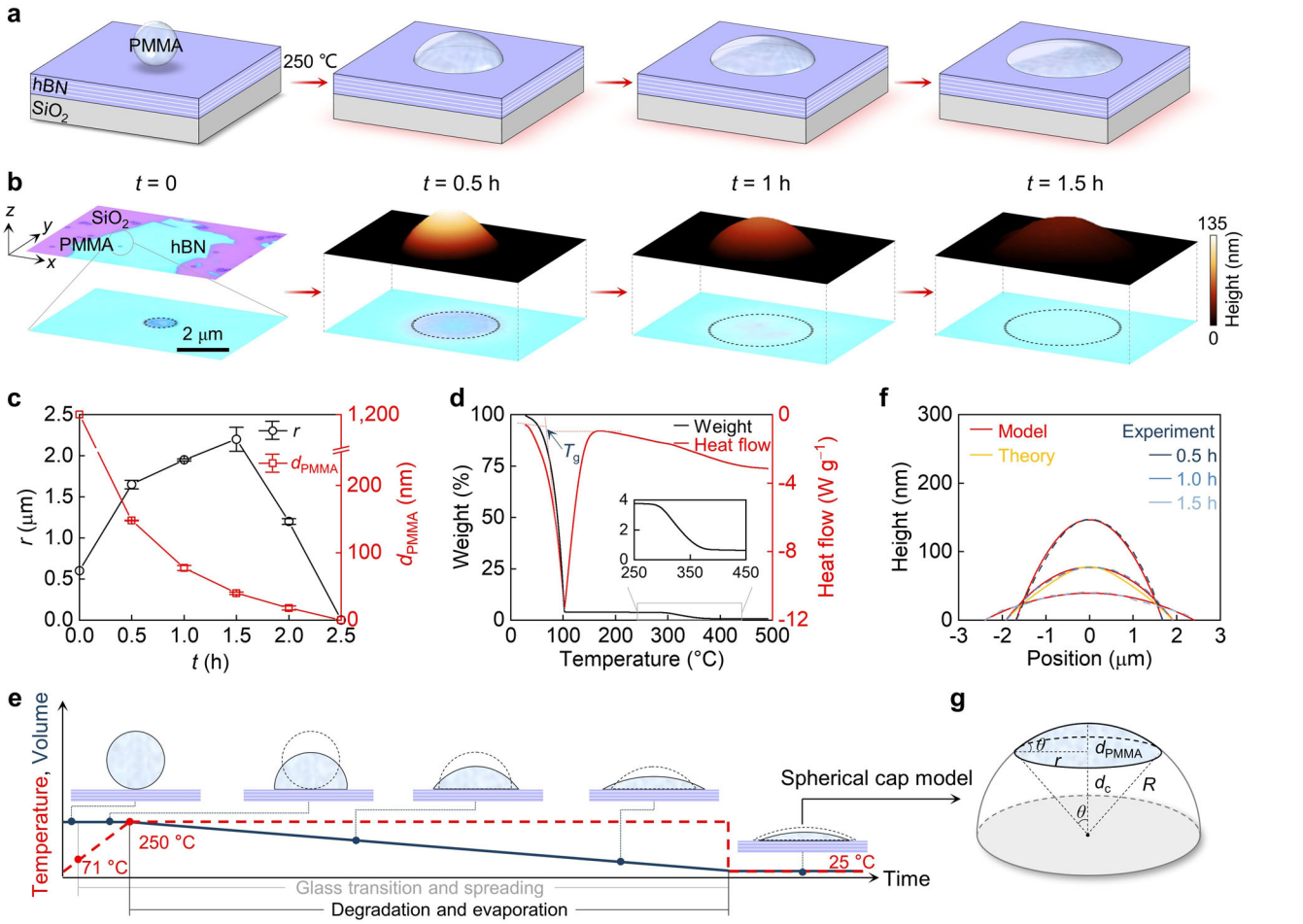

Fig. 3 | Lithography-free approach to modelling PMMA caps. a Schematic illustration of the melting process of a PMMA sphere on the hBN surface. **b** Optical images of a PMMA sphere at each stage, with black circles marking the outlines of PMMA. The top panel displays corresponding atomic force microscopy images. **c** Measured radii (r) and heights (d_{PMMA}) of the PMMA microstructure as a function of thermal treatment time (t). **d** Thermogravimetric analysis curve for the PMMA microsphere aqueous dispersion, with an inset zooming in on the evaporation of PMMA. The midpoint of the baseline step in heat flow determines the glass transition temperature (T_g). **e** Time-dependent temperature and volume diagram during thermal treatment. Top panel: schematic illustrations of representative morphologies at various stages, with grey dashed outlines indicating the previous stage for visual comparison. **f** Comparison of cross-sectional height profiles from experiments (blue), spherical cap models (red), and Luneburg lens theory (orange). **g** Sketch of a spherical cap within a hemisphere, with the radius of R. Because of the small aspect ratio of the PMMA microstructure ($d_{PMMA}/r \ll 1$), its corresponding spherical cap is near the apex of the hemisphere with a small contact angle (θ).

displayed in Fig. 3f (blue curves). Given the small aspect ratio of the obtained PMMA microstructures, where $d_{PMMA}/r \ll 1$ with r being the lateral radius, we employ a spherical cap model to describe the geometry of PMMA microstructures as a function of the lateral radial distance (r_d), defined by:

$$d_{PMMA}(r_d) = \sqrt{R^2 - {r_d}^2} - d_c \quad (2)$$

where $R = r/\sin(\theta)$ is the radius of the sphere, $d_c = \sqrt{R^2 - r^2}$ is the vertical distance between cap bottom and sphere centre, and θ represents the contact angle of the PMMA structure relative to the hBN surface, which is equal to half of the open angle of the spherical cap, as depicted in Fig. 3g. The calculated height profiles are represented by the red curves in Fig. 3f, which align well with experimental results. The fitting parameters are listed in Supplementary Table 1. This model offers a convenient means to predict and assess the evolution of PMMA microstructures during the controlled melting process.

Polaritonic lenses with gradient effective refractive indices

Our lithography-free and cost-effective method enables the in situ production of PMMA microstructures with variable height and controlled radius on the surfaces of polaritonic materials, facilitating the fabrication of polaritonic lenses with gradient n_{eff}. Taking the polaritonic Luneburg lens as an example, its refractive index distribution as a function of r_d resembles that of an optical Luneburg lens, expressed as $n_{eff}(r_d) = \sqrt{2 - (r_d/r)^2}$ [31,32]. Given its similar form to Eq. 2, such gradient indices are expected to be satisfied by the gradient height of our PMMA caps fabricated through our controllable melting method. Indeed, as shown in Fig. 3f, the as-prepared PMMA cap at $t = 1.0$ h closely matches the required geometry (orange curve) for a polaritonic Luneburg lens at $\omega = 1470\ cm^{-1}$.

We use scattering-type scanning near-field optical microscopy (s-SNOM) to image polariton propagation in real space. This technique uses a sharp, apertureless metallic tip for the simultaneous excitation and detection of polaritons, along with topographic mapping. The real part of the second-harmonic near-field signal, $Re(\sigma_2)$, for a polaritonic lens is indicated by false colour in Fig. 4a, which is overlapped on the three-dimensional topography of the structure with $d_{hBN} = 89$ nm. The cross-sectional height profile of the PMMA cap aligns well with the theoretical geometry for a polaritonic Luneburg lens at $1500\ cm^{-1}$, resulting in concave interference patterns and a focal spot near the

https://doi.org/10.1038/s41467-025-63097-8

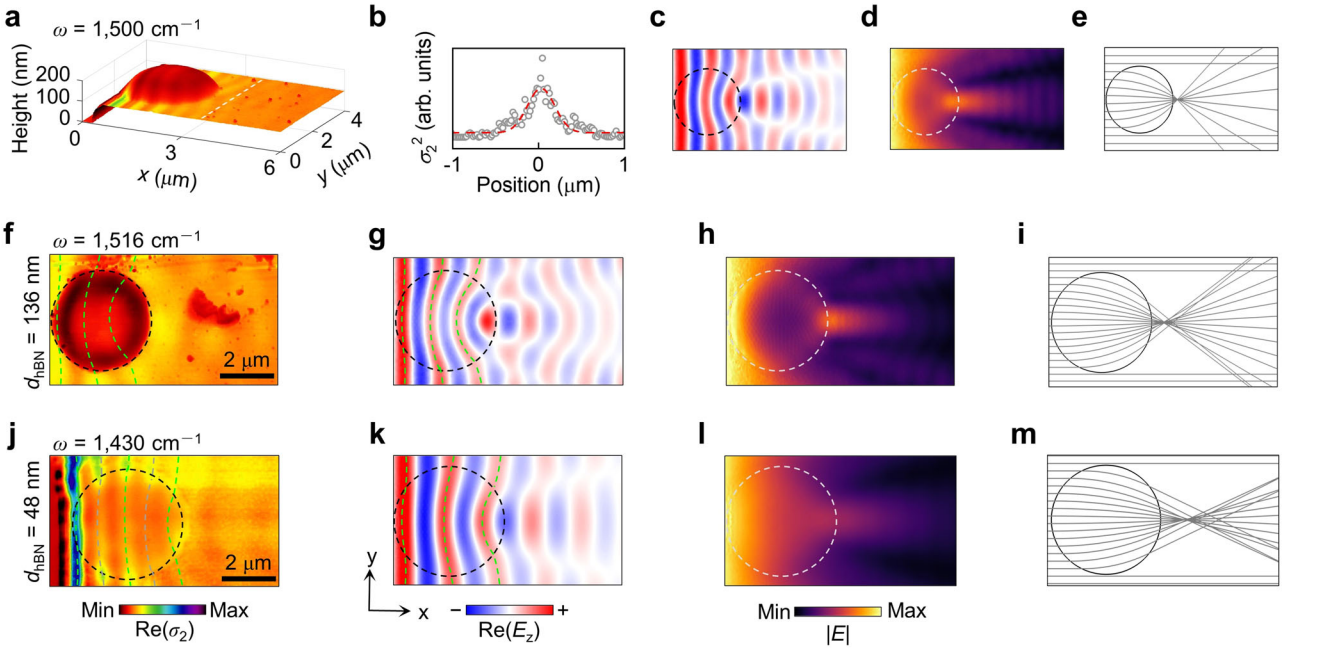

Fig. 4 | Polaritonic lenses with gradient effective refractive indices. a Near-field image (real part) of a polaritonic Lunrburg lens, Re(σ_2), at the frequency (ω) of 1500 cm^{-1}, overlapped on its three-dimensional topography, where the thickness of the hBN slab (d_{hBN}) is 89 nm. **b** Line scan signals along the focal spot and corresponding Gauss fitting. **c** Simulated field distribution in the x–y plane, denoted by the real part of the electric field in the z direction, Re(E_z). **d** Corresponding magnitude of the simulated electric field (|E|). **e** Ray-tracing result. Experimental (**f**) and simulated results (**g**–**i**) for another polaritonic Luneburg lens with a larger size. **j**–**m** Same as (**f**–**i**) but for a polaritonic lens with a gentler index distribution than that of a Luneburg lens. Green and grey curves indicate the concave interference patterns resulting from edge-launched and edge-reflected tip-launched polaritons, respectively.

lens rim when polaritons traverse PMMA. The focusing resolution, denoted by the full width at half maximum (FWHM) at the focal spot, is 0.38 μm, equal to $\lambda_0/18$ or $\lambda_p/3$ (Fig. 4b). Simulations of the electric field in Fig. 4c, d confirm the observed focusing behaviour. Ray-tracing results in Fig. 4e demonstrate how polariton beams bend through the PMMA cap, converging at a narrow focal spot near the lens rim. The slight offset of the focal position arises from the minor differences between theoretical and experimental geometries, which have a negligible impact on field distributions and lens properties, as compared with simulation results on theoretical structures in Supplementary Fig. 6.

The dimensions of the prepared PMMA caps can be conveniently adjusted by varying the size of the PMMA microsphere used in the fabrication process. Figure 4f presents a polaritonic Luneburg lens fabricated from a larger PMMA microsphere, yielding a larger focal spot with a resolution of 1.04 μm ($\lambda_0/6$), consistent with simulations in Fig. 4g–i. This decrease in resolution is due to the larger λ_p supported by the thicker hBN slab with d_{hBN} = 136 nm, indicating the essential role of polariton wavelength in the performance of polaritonic Luneburg lenses (Supplementary Note 2). The resolution can be improved by reducing hBN thicknesses or shifting frequencies, as demonstrated by the simulation results in Supplementary Fig. 7, where a resolution of $\lambda_0/39$ is achieved with a 30 nm-thick hBN slab at 1510 cm^{-1}.

Beyond polaritonic Luneburg lenses with pre-defined n_{eff} distributions, other polaritonic lenses with gradient n_{eff} can be realised by modifying the PMMA geometry or adjusting the operating frequency—two approaches that are functionally equivalent in shaping n_{eff}. As demonstrated in Fig. 4j–l, the concave interference patterns observed within the PMMA cap exhibit reduced curvature compared to those in Luneburg lenses due to a gentler n_{eff} gradient. Additional interference fringes (grey curves) appear in the near-field image, exhibiting a periodicity reduced to half that predicted by simulations. These features are attributed to edge-reflected polaritons launched by the tip (Supplementary Fig. 8). The focal spot in this lens is less distinct, which is caused by dispersive electric fields, as corroborated by the ray-tracing result in Fig. 4m. By contrast, a steeper n_{eff} gradient promotes rapid convergence, shifting the focal spot beneath the PMMA cap and thereby limiting its detectability in near-field measurements. To ensure clear identification of the focal spot, we deliberately choose a slightly lower n_{eff} than the ideal value in Fig. 4a. A comprehensive frequency-dependent evolution of the focusing behaviour is provided in Supplementary Fig. 9.

Our strategy is not limited to PMMA; other polymers, as well as organic or inorganic materials with predefined geometries and appropriate thermodynamic properties, could also be employed to serve as dielectric components and create gradient polaritonic lenses via our lithography-free approach. As a proof-of-concept demonstration, we prepared a gradient polaritonic lens using a polystyrene (PS) microsphere, following a similar procedure in Fig. 3a. Because of the slightly higher dielectric permittivity of PS ($\varepsilon_{PS} \approx 2.4$), the required PS geometry for a polaritonic Luneburg lens varies from that of PMMA. The theoretical geometry and refractive index are depicted by orange curves in Fig. 5a,b, which are satisfied excellently by the PS microstructure (blue curve) obtained by our lithography-free method and fitted by our spherical cap model. The near-field image of the fabricated device is shown in Fig. 5c, where the concave wavefronts over the PS region indicate gradually focused polaritons, culminating in a focal spot with a resolution of 0.52 μm ($\lambda_0/13$). These features are qualitatively reproduced by numerical simulations (Fig. 5d, e) and ray-tracing results (Fig. 5f). Additional PS-based lenses and corresponding near-field images are provided in Supplementary Fig. 10, demonstrating the reproducibility of our approach.

Discussion

Beyond polaritonic Luneburg lenses, our method is extendable to the fabrication of other gradient-index lenses with distinct functionalities. For instance, Maxwell fisheye lenses[40], which focus circular wavefronts from a point source to the lens rim, could be implemented using our

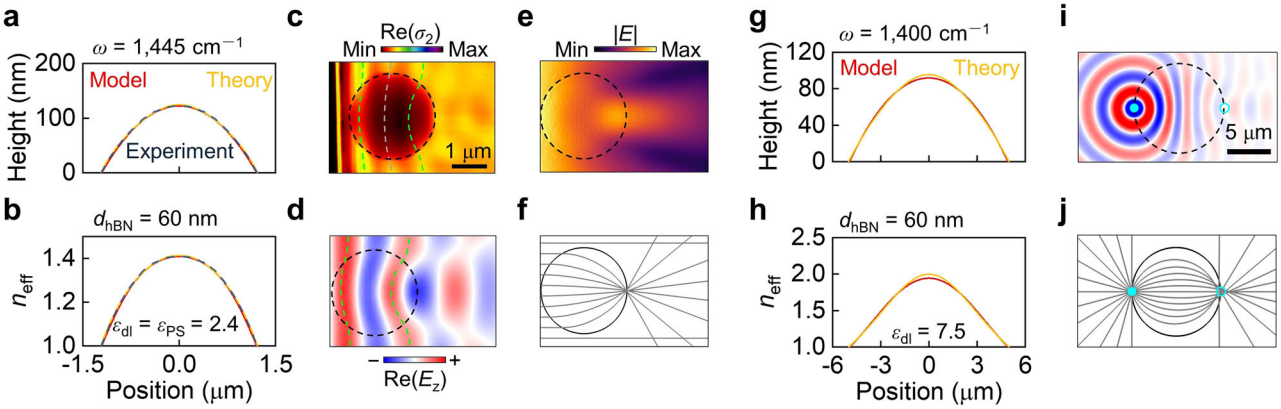

Fig. 5 | Lithography-free strategy for versatile polaritonic lenses. a Cross-sectional height profile of the prepared polystyrene (PS) cap (blue), aligning well with the spherical cap model (red) and theoretical Luneburg lens geometry (orange) at the frequency (ω) of 1445 cm^{-1}. The thickness of the hBN slab (d_{hBN}) is 60 nm. **b** Corresponding distribution of effective refractive indices (n_{eff}). **c** Near-field image (real part) of a polaritonic Lunrburg lens, Re(σ_2). Numerical simulation (**d, e**) and ray-tracing results (**f**). Cross-sectional height profile (**g**) and index distribution (**h**) of a proposed spherical cap atop an hBN slab, agreeing well with the required theoretical Maxwell fisheye lens. The permittivity of the dielectric layer (ε_{dl}) is set to 7.5. **i** Field distribution over the spherical cap excited by a *z*-polarised dipole (cyan dot), where a mirrored focal spot (cyan circle) at the opposite position of the lens rim is formed. (**j**) Ray-tracing result for the polaritonic Maxwell fisheye lens.

approach. The required n_{eff} distribution, $n_{eff}(r_d) = 2/[1 + (r_d/r)^2]$ [31], can be fulfilled by employing dielectric components with higher permittivities (Fig. 2e). The orange curves in Fig. 5g, h represent theoretical predictions for $\varepsilon_{dl} = 7.5$, which match closely with a spherical cap geometry characterised by $r = 4.9$ μm and $\theta = 2.1°$. This design is achievable using our lithography-free method with polymers such as polyvinylidene fluoride[41]. Full-wave simulations and ray tracing in Fig. 5i, j confirm the formation of a focused spot at the lens rim, yielding a resolution of $\lambda_0/3$, consistent with theoretical expectations (Supplementary Fig. 11).

Our framework assumes isotropic polaritons, where the wavevector and Poynting vector are colinear. However, in-plane anisotropic polaritons violate this condition[26], necessitating more sophisticated designs involving spatially varying index tensors and asymmetric geometries[30]. These configurations are currently beyond the capabilities of our approach, which is primarily based on gravity-driven spontaneous spreading, naturally favouring radially symmetric, isotropic configurations. That said, our method is not limited to radially symmetric lens geometries. As a proof of concept, we propose a polaritonic Mikaelian lens formed from a PMMA rod with a high length-to-diameter ratio. Supplementary Fig. 12 illustrates the lens geometry, where the circular cross-section is shaped through thermal treatment and accurately modelled using the cap approximation, while the longitudinal dimension remains unaffected. When excited by a point dipole positioned above the rod centre, this structure enables self-focusing of polaritons along the longitudinal axis, thereby functioning as a Mikaelian lens for in-plane isotropic polariton modes[42,43].

Our lithography-free approach, based on the reshaping of commercially available polymer microspheres, enables scalable fabrication of gradient-index polaritonic lenses. To ensure optimal lens performance, two design considerations are paramount: (i) the lens diameter must exceed at least two polariton fringe periods and maintain adequate signal intensity to allow for distinct focusing, and (ii) the spherical cap height should be minimised—provided that the n_{eff} requirements are satisfied—to promote efficient polariton penetration and detection.

In summary, we have demonstrated a simple, scalable, and cost-effective lithography-free approach for fabricating polaritonic Luneburg lenses and theoretically validated its generalizability to Maxwell fisheye and Mikaelian lens designs. It supports a wide range of polymers and is compatible with inorganic dielectrics and is readily transferable to diverse polaritonic material platforms, including metals[44], semiconductors[45], and graphene[46,47]. The latter, as shown in Supplementary Figs. 13, 14, offers a compelling pathway for realising gate-tunable gradient-index lenses via electrostatic doping. Future efforts will focus on improving control over the deposition process using techniques such as tip sliding[48] or inkjet printing[49]. Moreover, mitigating polariton losses through strategies such as isotope purification[50,51], cryogenic cooling[52–54], and suspended architectures[55–57] may enhance the field intensity at focal spots, thereby enabling larger-area lenses with improved performance.

Methods

Sample fabrication

HBN slabs with varying thicknesses were mechanically exfoliated from bulk hBN crystals (HQ Graphene) and transferred onto SiO_2/Si substrates. PMMA microsphere aqueous dispersions (50 mg mL^{-1}) were purchased from Beijing Zhongke Keyou Technology Co., Ltd. The radii of PMMA microspheres, synthesised via suspension polymerisation, can be tailored from 100 nm to 100 μm, with number-average molecular weights between 80,000 and 120,000.

To prepare a diluted suspension, a drop (≈0.05 mL) of the stock suspension was added to 40 mL of isopropanol. This diluted suspension was then drop-cast onto hBN slabs. A low concentration of microspheres was used to minimise aggregation during deposition. The deposition process was repeated as necessary to ensure microspheres were positioned appropriately on the hBN surface.

Following air drying, the samples were placed in a tube furnace preheated to 250 °C in an ambient air atmosphere. The duration of the thermal treatment was adjusted based on the microsphere size and hBN slab thickness (Supplementary Fig. 5). Upon completion, the samples were removed from the hot furnace and allowed to cool naturally in air. During cooling, the softened PMMA re-solidified into flattened caps. This heating–cooling cycle was repeated as needed to achieve the desired cap geometry. Structures composed of PS (purchased from Beijing Zhongke Keyou Technology Co., Ltd.) were prepared following a similar procedure under the same thermal treatment temperature.

Material characterization

Thermogravimetric analysis test of the as-purchased suspension was performed using Discovery SDT 650 (TA Instruments) in an air atmosphere at a heating rate of 10 °C min^{-1}. The topographical images shown in Fig. 3b were obtained with atomic force microscopy

(DimensionXR, Bruker). To account for geometric imperfections, the radii and heights of the PMMA microstructures depicted in Fig. 3c were extracted and averaged from four line scans through the centre in various directions.

Near-field optical imaging was conducted using a commercially integrated s-SNOM system (neaSNOM, Neaspec). A PtIr-coated atomic force microscope tip (Arrow-NCPt, NanoWorld) served as the scattering near-field probe, enabling simultaneous acquisition of the sample's topography during imaging. During s-SNOM scanning, the tip oscillated vertically with an amplitude of ~60 nm at a frequency of ~273 kHz. Illumination was provided by a wavelength-tunable, continuous-wave quantum cascade laser (MIRcat, Daylight Solutions). The backscattered signals were recorded using a pseudo-heterodyne Michelson interferometer and demodulated at the second harmonic of the tip oscillation frequency. The complex-valued near-field signals (σ) were calculated from the recorded amplitude (s) and phase signals (φ) using the equation $\sigma = se^{i\varphi}$.

Numerical simulation

Electromagnetic field simulations were performed using the wave optics module in COMSOL Multiphysics. The model geometries illustrated in Fig. 4 were constructed based on experimental results. A plane wave incident from the left side of the model served as the source to excite polaritons. This configuration produced interference patterns with double the periodicity observed in the experimental near-field images if the measured polaritons primarily consist of edge-reflected signals launched by the tip[31]. The electric field in Fig. 5i was excited by a z-polarised point dipole at the lens rim.

Data availability

The data that support the findings of this study are available within the paper and Supplementary Information. The raw near-field data have been deposited in the figshare database under accession code https://doi.org/10.6084/m9.figshare.29618924.

Code availability

The details of the simulations are described in Supplementary Information. Additional information that supports the findings of this study is available from the corresponding authors upon request.

References

1. Maier, S. A. *Plasmonics: Fundamentals and applications*. (Springer, Berlin, 2007).
2. Basov, D. N., Fogler, M. M. & Garcia de Abajo, F. J. Polaritons in van der waals materials. *Science* **354**, aaag1992 (2016).
3. Low, T. et al. Polaritons in layered two-dimensional materials. *Nat. Mater.* **16**, 182–194 (2017).
4. Wu, Y. et al. Manipulating polaritons at the extreme scale in van der Waals materials. *Nat. Rev. Phys.* **4**, 578–594 (2022).
5. Barnes, W. L., Dereux, A. & Dereux, T. W. Surface plasmon subwavelength optics. *Nature* **424**, 824–830 (2003).
6. Zhang, Q. et al. Interface nano-optics with van der Waals polaritons. *Nature* **597**, 187–195 (2021).
7. Galiffi, E. et al. Extreme light confinement and control in low-symmetry phonon-polaritonic crystals. *Nat. Rev. Mater.* **9**, 9–28 (2024).
8. Alfaro-Mozaz, F. J. et al. Nanoimaging of resonating hyperbolic polaritons in linear boron nitride antennas. *Nat. Commun.* **8**, 15624 (2017).
9. Dunkelberger, A. D. et al. Active tuning of surface phonon polariton resonances via carrier photoinjection. *Nat. Photonics* **12**, 50–56 (2018).
10. Autore, M. et al. Boron nitride nanoresonators for phonon-enhanced molecular vibrational spectroscopy at the strong coupling limit. *Light Sci. Appl.* **7**, 17172 (2018).
11. Lee, I. H., Yoo, D., Avouris, P., Low, T. & Oh, S. H. Graphene acoustic plasmon resonator for ultrasensitive infrared spectroscopy. *Nat. Nanotechnol.* **14**, 313–319 (2019).
12. Autore, M. et al. Enhanced light–matter interaction in ^{10}B monoisotopic boron nitride infrared nanoresonators. *Adv. Opt. Mater.* **9**, 2001958 (2020).
13. Duan, J. et al. Active and passive tuning of ultranarrow resonances in polaritonic nanoantennas. *Adv. Mater.* **34**, e2104954 (2022).
14. Yu, S. J. et al. Ultrahigh-quality infrared polaritonic resonators based on bottom-up-synthesized van der Waals nanoribbons. *ACS Nano* **16**, 3027–3035 (2022).
15. Dolado, I. et al. Nanoscale guiding of infrared light with hyperbolic volume and surface polaritons in van der Waals material ribbons. *Adv. Mater.* **32**, e1906530 (2020).
16. He, M. et al. Guided mid-IR and near-IR light within a hybrid hyperbolic-material/silicon waveguide heterostructure. *Adv. Mater.* **33**, e2004305 (2021).
17. Zhao, W. et al. Nanoimaging of low-loss plasmonic waveguide modes in a graphene nanoribbon. *Nano Lett.* **21**, 3106–3111 (2021).
18. He, M. et al. Guided polaritons along the forbidden direction in MoO_3 with geometrical confinement. *Nano Lett.* **23**, 5035–5041 (2023).
19. Alonso-Gonzalez, P. et al. Controlling graphene plasmons with resonant metal antennas and spatial conductivity patterns. *Science* **344**, 1369–1373 (2014).
20. Chaudhary, K. et al. Polariton nanophotonics using phase-change materials. *Nat. Commun.* **10**, 4487 (2019).
21. Zhao, Y. et al. Tunable heterostructural prism for planar polaritonic switch. *Sci. Bull.* **68**, 1757–1763 (2023).
22. Martín-Sánchez, J. et al. Focusing of in-plane hyperbolic polaritons in van der Waals crystals with tailored infrared nanoantennas. *Sci. Adv.* **7**, eabj0127 (2021).
23. Zheng, Z. et al. Controlling and focusing in-plane hyperbolic phonon polaritons in α-MoO_3 with a curved plasmonic antenna. *Adv. Mater.* **34**, e2104164 (2022).
24. Qu, Y. et al. Tunable planar focusing based on hyperbolic phonon polaritons in α-MoO_3. *Adv. Mater.* **34**, e2105590 (2022).
25. Liang, J. et al. Manipulation of in-plane hyperbolic phonon polaritons for configurable focusing. *ACS Photonics* **11**, 5031–5038 (2024).
26. Duan, J. et al. Planar refraction and lensing of highly confined polaritons in anisotropic media. *Nat. Commun.* **12**, 4325 (2021).
27. Hu, H. et al. Doping-driven topological polaritons in graphene/α-MoO_3 heterostructures. *Nat. Nanotechnol.* **17**, 940–946 (2022).
28. Hu, H. et al. Gate-tunable negative refraction of mid-infrared polaritons. *Science* **379**, 558–561 (2023).
29. He, Z. et al. Reflectionless refraction via one-dimensional ghost polaritons in planar junctions of hyperbolic metasurfaces. *Prog. Electromagn. Res.* **181**, 1–8 (2024).
30. Tao, S. Anisotropic Fermat's principle for controlling hyperbolic van der Waals polaritons. *Photonics Res* **10**, B14–B22 (2022).
31. Wu, Y. et al. Monolithically structured van der Waals materials for volume-polariton refraction and focusing. *ACS Nano* **18**, 17065–17074 (2024).
32. Liu, Y., Zentgraf, T., Bartal, G. & Zhang, X. Transformational plasmon optics. *Nano Lett.* **10**, 1991–1997 (2010).
33. Huidobro, P. A., Nesterov, M. L., Martin-Moreno, L. & Garcia-Vidal, F. J. Transformation optics for plasmonics. *Nano Lett.* **10**, 1985–1990 (2010).
34. Zentgraf, T., Liu, Y., Mikkelsen, M. H., Valentine, J. & Zhang, X. Plasmonic luneburg and eaton lenses. *Nat. Nanotechnol.* **6**, 151–155 (2011).
35. Ehlermann, J., Vu, H. & Mendach, S. Near field investigation of a plasmonic lüneburg lens. *Plasmonics* **10**, 1513–1518 (2015).

36. Garcia-Ortiz, C. E. et al. Plasmonic metasurface luneburg lens. *Photonics Res* **7**, 1112–1118 (2019).
37. Xu, H., Lu, W., Zhu, W., Dong, Z. & Cui, T. Efficient manipulation of surface plasmon polariton waves in graphene. *Appl. Phys. Lett.* **100**, 243110 (2012).
38. Feng, S. et al. Glass transition of poly(methyl methacrylate) nanospheres in aqueous dispersion. *Phys. Chem. Chem. Phys.* **16**, 15941–15947 (2014).
39. Lohse, D. & Zhang, X. H. Physicochemical hydrodynamics of droplets out of equilibrium. *Nat. Rev. Phys.* **2**, 426–443 (2020).
40. Zhou, Y., Hao, Z., Zhao, P. & Chen, H. Solid immersion Maxwell's fish-eye lens without drain. *Phys. Rev. Appl.* **17**, 034039 (2022).
41. Garg, T. et al. Dielectric properties and phase stabilization of PVDF polymer in (1–*x*)PVDF/*x*BCZT composite films. *J. Electron. Mater.* **50**, 5567–5576 (2021).
42. Wang, X. et al. Self-focusing and the Talbot effect in conformal transformation optics. *Phys. Rev. Lett.* **119**, 033902 (2017).
43. Hou, T., Xiao, W. & Chen, H. Cosmology analogy for perfect hyperlens. *npj. Nanophoton.* **2**, 16 (2025).
44. Abd El-Fattah, Z. M. et al. Plasmonics in atomically thin crystalline silver films. *ACS Nano* **13**, 7771–7779 (2019).
45. Sternbach, A. J. et al. Programmable hyperbolic polaritons in van der waals semiconductors. *Science* **371**, 617–620 (2021).
46. Chen, J. et al. Optical nano-imaging of gate-tunable graphene plasmons. *Nature* **487**, 77–81 (2012).
47. Fei, Z. et al. Gate-tuning of graphene plasmons revealed by infrared nano-imaging. *Nature* **487**, 82–85 (2012).
48. Ribeiro-Palau, R. et al. Twistable electronics with dynamically rotatable heterostructures. *Science* **361**, 690–693 (2018).
49. Singh, M., Haverinen, H. M., Dhagat, P. & Jabbour, G. E. Inkjet printing-process and its applications. *Adv. Mater.* **22**, 673–685 (2010).
50. Giles, A. J. et al. Ultralow-loss polaritons in isotopically pure boron nitride. *Nat. Mater.* **17**, 134–139 (2018).
51. Zhao, Y. et al. Ultralow-loss phonon polaritons in the isotope-enriched α-MoO_3. *Nano Lett.* **22**, 10208–10215 (2022).
52. Ni, G. X. et al. Fundamental limits to graphene plasmonics. *Nature* **557**, 530–533 (2018).
53. Ni, G. X. et al. Long-lived phonon polaritons in hyperbolic materials. *Nano Lett.* **21**, 5767–5773 (2021).
54. Voronin, K. V., Alvarez-Pérez, G., Lanza, C. S., Alonso-González, P. & Nikitin, A. Y. Fundamentals of polaritons in strongly anisotropic thin crystal layers. *ACS Photonics* **11**, 550–560 (2024).
55. Dai, S. et al. Hyperbolic phonon polaritons in suspended hexagonal boron nitride. *Nano Lett.* **19**, 1009–1014 (2019).
56. Zheng, Z. et al. Tunable hyperbolic phonon polaritons in a suspended van der Waals α-MoO_3 with gradient gaps. *Adv. Opt. Mater.* **10**, 2102057 (2021).
57. Hu, H. et al. Active control of micrometer plasmon propagation in suspended graphene. *Nat. Commun.* **13**, 1465 (2022).

Acknowledgements

Y.W. and H.C. are supported by the National Natural Science Foundation of China (62275231, 62305288), the Key Research and Development Program of the Ministry of Science and Technology (2022YFA1404704, 2022YFA1405200, 2022YFA1404902), the Key Research and Development Program of Zhejiang Province (2024C01160), and the Fundamental Research Funds for the Central Universities. Y.W. and B.Z. acknowledge support from Zhejiang Provincial Natural Science Foundation of China (LZ25F050002, LR23F010004), the Top-Notch Young Talent of China and Top-Notch Young Talent of Zhejiang Province. Y.G. and Y.Z. acknowledge support from the National Natural Science Foundation of China (62305228, 62375179), and the Science and Technology Innovation Commission of Shenzhen (RCYX20210609103709024, JCYJ20240813141208011). W.M. acknowledges the funding support from the National Natural Science Foundation of China (52402020), as well as the Central Government-Guided Program for Science and Technology Development (2024ZYD0082).

Author contributions

Y.W. conceived the idea. Z.C. prepared samples, analysed experimental data, and performed theoretical analysis and numerical simulations with the help of W.Y., S.X., Z.H., X.T., B.Z., H.W., W.M., and Y.W. Y.G. carried out near-field measurements. Z.C., Y.G., and Y.W. co-wrote the manuscript with inputs from all the other authors. Y.Z., H.C., and Y.W. supervised the project.

Competing interests

The authors declare no competing interests.

Additional information

Supplementary information The online version contains supplementary material available at https://doi.org/10.1038/s41467-025-63097-8.

Correspondence and requests for materials should be addressed to Yupeng Zhang, Hongsheng Chen or Yingjie Wu.

Peer review information *Nature Communications* thanks the anonymous reviewer(s) for their contribution to the peer review of this work. A peer review file is available.